

Measurement of direct photon pair production cross sections in $p\bar{p}$ collisions at $\sqrt{s} = 1.96$ TeV

V.M. Abazov³⁶, B. Abbott⁷⁴, M. Abolins⁶³, B.S. Acharya²⁹, M. Adams⁴⁹, T. Adams⁴⁷, E. Aguilo⁶, G.D. Alexeev³⁶, G. Alkhazov⁴⁰, A. Alton^{62,a}, G. Alverson⁶¹, G.A. Alves², L.S. Ancu³⁵, M. Aoki⁴⁸, Y. Arnaud¹⁴, M. Arov⁵⁸, A. Askew⁴⁷, B. Åsman⁴¹, O. Atramentov⁶⁶, C. Avila⁸, J. BackusMayes⁸¹, F. Badaud¹³, L. Bagby⁴⁸, B. Baldin⁴⁸, D.V. Bandurin⁴⁷, S. Banerjee²⁹, E. Barberis⁶¹, A.-F. Barfuss¹⁵, P. Baringer⁵⁶, J. Barreto², J.F. Bartlett⁴⁸, U. Bässler¹⁸, S. Beale⁶, A. Bean⁵⁶, M. Begalli³, M. Begel⁷², C. Belanger-Champagne⁴¹, L. Bellantoni⁴⁸, J.A. Benitez⁶³, S.B. Beri²⁷, G. Bernardi¹⁷, R. Bernhard²², I. Bertram⁴², M. Besançon¹⁸, R. Beuselinck⁴³, V.A. Bezzubov³⁹, P.C. Bhat⁴⁸, V. Bhatnagar²⁷, G. Blazey⁵⁰, S. Blessing⁴⁷, K. Bloom⁶⁵, A. Boehnlein⁴⁸, D. Boline⁶⁰, T.A. Bolton⁵⁷, E.E. Boos³⁸, G. Borissov⁴², T. Bose⁶⁰, A. Brandt⁷⁷, R. Brock⁶³, G. Brooijmans⁶⁹, A. Bross⁴⁸, D. Brown¹⁹, X.B. Bu⁷, D. Buchholz⁵¹, M. Buehler⁸⁰, V. Buescher²⁴, V. Bunichev³⁸, S. Burdin^{42,b}, T.H. Burnett⁸¹, C.P. Buszello⁴³, P. Calfayan²⁵, B. Calpas¹⁵, S. Calvet¹⁶, E. Camacho-Pérez³³, J. Cammin⁷⁰, M.A. Carrasco-Lizarraga³³, E. Carrera⁴⁷, B.C.K. Casey⁴⁸, H. Castilla-Valdez³³, S. Chakrabarti⁷¹, D. Chakraborty⁵⁰, K.M. Chan⁵⁴, A. Chandra⁷⁹, G. Chen⁵⁶, S. Chevalier-Théry¹⁸, D.K. Cho⁷⁶, S.W. Cho³¹, S. Choi³², B. Choudhary²⁸, T. Christoudias⁴³, S. Cihangir⁴⁸, D. Claes⁶⁵, J. Clutter⁵⁶, M. Cooke⁴⁸, W.E. Cooper⁴⁸, M. Corcoran⁷⁹, F. Couderc¹⁸, M.-C. Cousinou¹⁵, D. Cutts⁷⁶, M. Ćwiok³⁰, A. Das⁴⁵, G. Davies⁴³, K. De⁷⁷, S.J. de Jong³⁵, E. De La Cruz-Burelo³³, K. DeVaughan⁶⁵, F. Déliot¹⁸, M. Demarteau⁴⁸, R. Demina⁷⁰, D. Denisov⁴⁸, S.P. Denisov³⁹, S. Desai⁴⁸, H.T. Diehl⁴⁸, M. Diesburg⁴⁸, A. Dominguez⁶⁵, T. Dorland⁸¹, A. Dubey²⁸, L.V. Dudko³⁸, L. Dufлот¹⁶, D. Duggan⁶⁶, A. Duperrin¹⁵, S. Dutt²⁷, A. Dyshkant⁵⁰, M. Eads⁶⁵, D. Edmunds⁶³, J. Ellison⁴⁶, V.D. Elvira⁴⁸, Y. Enari¹⁷, S. Eno⁵⁹, H. Evans⁵², A. Evdokimov⁷², V.N. Evdokimov³⁹, G. Facini⁶¹, A.V. Ferapontov⁷⁶, T. Ferbel^{59,70}, F. Fiedler²⁴, F. Filthaut³⁵, W. Fisher⁶³, H.E. Fisk⁴⁸, M. Fortner⁵⁰, H. Fox⁴², S. Fuess⁴⁸, T. Gadfort⁷², A. Garcia-Bellido⁷⁰, V. Gavrilov³⁷, P. Gay¹³, W. Geist⁴⁹, W. Geng^{15,63}, D. Gerbaudo⁶⁷, C.E. Gerber⁴⁹, Y. Gershtein⁶⁶, D. Gillberg⁶, G. Ginther^{48,70}, G. Golovanov³⁶, B. Gómez⁸, A. Goussiou⁸¹, P.D. Grannis⁷¹, S. Greder¹⁹, H. Greenlee⁴⁸, Z.D. Greenwood⁵⁸, E.M. Gregores⁴, G. Grenier²⁰, Ph. Gris¹³, J.-F. Grivaz¹⁶, A. Grohsjean¹⁸, S. Grünendahl⁴⁸, M.W. Grünewald³⁰, F. Guo⁷¹, J. Guo⁷¹, G. Gutierrez⁴⁸, P. Gutierrez⁷⁴, A. Haas^{69,c}, P. Haefner²⁵, S. Hagopian⁴⁷, J. Haley⁶¹, I. Hall⁶³, L. Han⁷, K. Harder⁴⁴, A. Harel⁷⁰, J.M. Hauptman⁵⁵, J. Hays⁴³, T. Hebbeker²¹, D. Hedin⁵⁰, A.P. Heinson⁴⁶, U. Heintz⁷⁶, C. Hensel²³, I. Heredia-De La Cruz³³, K. Herner⁶², G. Hesketh⁶¹, M.D. Hildreth⁵⁴, R. Hirosky⁸⁰, T. Hoang⁴⁷, J.D. Hobbs⁷¹, B. Hoeneisen¹², M. Hohlfeld²⁴, S. Hossain⁷⁴, P. Houben³⁴, Y. Hu⁷¹, Z. Hubacek¹⁰, N. Huske¹⁷, V. Hynek¹⁰, I. Iashvili⁶⁸, R. Illingworth⁴⁸, A.S. Ito⁴⁸, S. Jabeen⁷⁶, M. Jaffré¹⁶, S. Jain⁶⁸, D. Jamin¹⁵, R. Jesik⁴³, K. Johns⁴⁵, C. Johnson⁶⁹, M. Johnson⁴⁸, D. Johnston⁶⁵, A. Jonckheere⁴⁸, P. Jonsson⁴³, A. Juste^{48,d}, E. Kajfasz¹⁵, D. Karmanov³⁸, P.A. Kasper⁴⁸, I. Katsanos⁶⁵, R. Kehoe⁷⁸, S. Kermiche¹⁵, N. Khalatyan⁴⁸, A. Khanov⁷⁵, A. Kharchilava⁶⁸, Y.N. Kharzhev³⁶, D. Khatidze⁷⁶, M.H. Kirby⁵¹, M. Kirsch²¹, J.M. Kohli²⁷, A.V. Kozelov³⁹, J. Kraus⁶³, A. Kumar⁶⁸, A. Kupco¹¹, T. Kurča²⁰, V.A. Kuzmin³⁸, J. Kvita⁹, S. Lammers⁵², G. Landsberg⁷⁶, P. Lebrun²⁰, H.S. Lee³¹, W.M. Lee⁴⁸, J. Lellouch¹⁷, L. Li⁴⁶, Q.Z. Li⁴⁸, S.M. Lietti⁵, J.K. Lim³¹, D. Lincoln⁴⁸, J. Linnemann⁶³, V.V. Lipaev³⁹, R. Lipton⁴⁸, Y. Liu⁷, Z. Liu⁶, A. Lobodenko⁴⁰, M. Lokajicek¹¹, P. Love⁴², H.J. Lubatti⁸¹, R. Luna-Garcia^{33,e}, A.L. Lyon⁴⁸, A.K.A. Maciel², D. Mackin⁷⁹, R. Magaña-Villalba³³, P.K. Mal⁴⁵, S. Malik⁶⁵, V.L. Malyshev³⁶, Y. Maravin⁵⁷, J. Martínez-Ortega³³, R. McCarthy⁷¹, C.L. McGivern⁵⁶, M.M. Meijer³⁵, A. Melnitchouk⁶⁴, L. Mendoza⁸, D. Menezes⁵⁰, P.G. Mercadante⁴, M. Merkin³⁸, A. Meyer²¹, J. Meyer²³, N.K. Mondal²⁹, T. Moulik⁵⁶, G.S. Muanza¹⁵, M. Mulhearn⁸⁰, E. Nagy¹⁵, M. Naimuddin²⁸, M. Narain⁷⁶, R. Nayyar²⁸, H.A. Neal⁶², J.P. Negret⁸, P. Neustroev⁴⁰, H. Nilsen²², S.F. Novaes⁵, T. Nunnemann²⁵, G. Obrant⁴⁰, D. Onoprienko⁵⁷, J. Orduna³³, N. Osman⁴³, J. Osta⁵⁴, G.J. Otero y Garzón¹, M. Owen⁴⁴, M. Padilla⁴⁶, M. Pangilinan⁷⁶, N. Parashar⁵³, V. Parihar⁷⁶, S.-J. Park²³, S.K. Park³¹, J. Parsons⁶⁹, R. Partridge⁷⁶, N. Parua⁵², A. Patwa⁷², B. Penning⁴⁸, M. Perfilov³⁸, K. Peters⁴⁴, Y. Peters⁴⁴, P. Pétrouff¹⁶, R. Piegaia¹, J. Piper⁶³, M.-A. Pleier⁷², P.L.M. Podesta-Lerma^{33,f}, V.M. Podstavkov⁴⁸, M.-E. Pol², P. Polozov³⁷, A.V. Popov³⁹, M. Prewitt⁷⁹, D. Price⁵², S. Protopopescu⁷², J. Qian⁶², A. Quadt²³, B. Quinn⁶⁴, M.S. Rangel¹⁶, K. Ranjan²⁸, P.N. Ratoff⁴², I. Razumov³⁹, P. Renkel⁷⁸, P. Rich⁴⁴, M. Rijssenbeek⁷¹, I. Ripp-Baudot¹⁹, F. Rizatdinova⁷⁵, M. Rominsky⁴⁸, C. Royon¹⁸, P. Rubinov⁴⁸, R. Ruchti⁵⁴, G. Safronov³⁷, G. Sajot¹⁴, A. Sánchez-Hernández³³, M.P. Sanders²⁵, B. Sanghi⁴⁸, G. Savage⁴⁸, L. Sawyer⁵⁸, T. Scanlon⁴³, D. Schaile²⁵, R.D. Schamberger⁷¹, Y. Scheglov⁴⁰, H. Schellman⁵¹,

T. Schliephake²⁶, S. Schlobohm⁸¹, C. Schwanenberger⁴⁴, R. Schwienhorst⁶³, J. Sekaric⁵⁶, H. Severini⁷⁴, E. Shabalina²³, V. Shary¹⁸, A.A. Shchukin³⁹, R.K. Shivpuri²⁸, V. Simak¹⁰, V. Sirotenko⁴⁸, P. Skubic⁷⁴, P. Slattery⁷⁰, D. Smirnov⁵⁴, G.R. Snow⁶⁵, J. Snow⁷³, S. Snyder⁷², S. Söldner-Rembold⁴⁴, L. Sonnenschein²¹, A. Sopczak⁴², M. Sosebee⁷⁷, K. Soustruznik⁹, B. Spurlock⁷⁷, J. Stark¹⁴, V. Stolin³⁷, D.A. Stoyanova³⁹, M.A. Strang⁶⁸, E. Strauss⁷¹, M. Strauss⁷⁴, R. Ströhmer²⁵, D. Strom⁴⁹, L. Stutte⁴⁸, P. Svoisky³⁵, M. Takahashi⁴⁴, A. Tanasijczuk¹, W. Taylor⁶, B. Tiller²⁵, M. Titov¹⁸, V.V. Tokmenin³⁶, D. Tsybychev⁷¹, B. Tuchming¹⁸, C. Tully⁶⁷, P.M. Tuts⁶⁹, R. Unalan⁶³, L. Uvarov⁴⁰, S. Uvarov⁴⁰, S. Uzunyan⁵⁰, R. Van Kooten⁵², W.M. van Leeuwen³⁴, N. Varelas⁴⁹, E.W. Varnes⁴⁵, I.A. Vasilyev³⁹, P. Verdier²⁰, L.S. Vertogradov³⁶, M. Verzocchi⁴⁸, M. Vesterinen⁴⁴, D. Vilanova¹⁸, P. Vint⁴³, P. Vokac¹⁰, H.D. Wahl⁴⁷, M.H.L.S. Wang⁷⁰, J. Warchol⁵⁴, G. Watts⁸¹, M. Wayne⁵⁴, G. Weber²⁴, M. Weber^{48,g}, M. Wetstein⁵⁹, A. White⁷⁷, D. Wicke²⁴, M.R.J. Williams⁴², G.W. Wilson⁵⁶, S.J. Wimpenny⁴⁶, M. Wobisch⁵⁸, D.R. Wood⁶¹, T.R. Wyatt⁴⁴, Y. Xie⁴⁸, C. Xu⁶², S. Yacoub⁵¹, R. Yamada⁴⁸, W.-C. Yang⁴⁴, T. Yasuda⁴⁸, Y.A. Yatsunenko³⁶, Z. Ye⁴⁸, H. Yin⁷, K. Yip⁷², H.D. Yoo⁷⁶, S.W. Youn⁴⁸, J. Yu⁷⁷, S. Zelitch⁸⁰, T. Zhao⁸¹, B. Zhou⁶², J. Zhu⁷¹, M. Zielinski⁷⁰, D. Zieminska⁵², and L. Zivkovic⁶⁹

(The DØ Collaboration)

¹Universidad de Buenos Aires, Buenos Aires, Argentina

²LAFEX, Centro Brasileiro de Pesquisas Físicas, Rio de Janeiro, Brazil

³Universidade do Estado do Rio de Janeiro, Rio de Janeiro, Brazil

⁴Universidade Federal do ABC, Santo André, Brazil

⁵Instituto de Física Teórica, Universidade Estadual Paulista, São Paulo, Brazil

⁶Simon Fraser University, Burnaby, British Columbia,

Canada; and York University, Toronto, Ontario, Canada

⁷University of Science and Technology of China, Hefei, People's Republic of China

⁸Universidad de los Andes, Bogotá, Colombia

⁹Center for Particle Physics, Charles University,

Faculty of Mathematics and Physics, Prague, Czech Republic

¹⁰Czech Technical University in Prague, Prague, Czech Republic

¹¹Center for Particle Physics, Institute of Physics,

Academy of Sciences of the Czech Republic, Prague, Czech Republic

¹²Universidad San Francisco de Quito, Quito, Ecuador

¹³LPC, Université Blaise Pascal, CNRS/IN2P3, Clermont, France

¹⁴LPSC, Université Joseph Fourier Grenoble 1, CNRS/IN2P3,

Institut National Polytechnique de Grenoble, Grenoble, France

¹⁵CPPM, Aix-Marseille Université, CNRS/IN2P3, Marseille, France

¹⁶LAL, Université Paris-Sud, IN2P3/CNRS, Orsay, France

¹⁷LPNHE, Universités Paris VI and VII, CNRS/IN2P3, Paris, France

¹⁸CEA, Irfu, SPP, Saclay, France

¹⁹IPHC, Université de Strasbourg, CNRS/IN2P3, Strasbourg, France

²⁰IPNL, Université Lyon 1, CNRS/IN2P3, Villeurbanne, France and Université de Lyon, Lyon, France

²¹III. Physikalisches Institut A, RWTH Aachen University, Aachen, Germany

²²Physikalisches Institut, Universität Freiburg, Freiburg, Germany

²³II. Physikalisches Institut, Georg-August-Universität Göttingen, Göttingen, Germany

²⁴Institut für Physik, Universität Mainz, Mainz, Germany

²⁵Ludwig-Maximilians-Universität München, München, Germany

²⁶Fachbereich Physik, University of Wuppertal, Wuppertal, Germany

²⁷Panjab University, Chandigarh, India

²⁸Delhi University, Delhi, India

²⁹Tata Institute of Fundamental Research, Mumbai, India

³⁰University College Dublin, Dublin, Ireland

³¹Korea Detector Laboratory, Korea University, Seoul, Korea

³²SungKyunKwan University, Suwon, Korea

³³CINVESTAV, Mexico City, Mexico

³⁴FOM-Institute NIKHEF and University of Amsterdam/NIKHEF, Amsterdam, The Netherlands

³⁵Radboud University Nijmegen/NIKHEF, Nijmegen, The Netherlands

³⁶Joint Institute for Nuclear Research, Dubna, Russia

³⁷Institute for Theoretical and Experimental Physics, Moscow, Russia

³⁸Moscow State University, Moscow, Russia

³⁹Institute for High Energy Physics, Protvino, Russia

⁴⁰Petersburg Nuclear Physics Institute, St. Petersburg, Russia

⁴¹Stockholm University, Stockholm, Sweden, and Uppsala University, Uppsala, Sweden

- ⁴²Lancaster University, Lancaster LA1 4YB, United Kingdom
⁴³Imperial College London, London SW7 2AZ, United Kingdom
⁴⁴The University of Manchester, Manchester M13 9PL, United Kingdom
⁴⁵University of Arizona, Tucson, Arizona 85721, USA
⁴⁶University of California Riverside, Riverside, California 92521, USA
⁴⁷Florida State University, Tallahassee, Florida 32306, USA
⁴⁸Fermi National Accelerator Laboratory, Batavia, Illinois 60510, USA
⁴⁹University of Illinois at Chicago, Chicago, Illinois 60607, USA
⁵⁰Northern Illinois University, DeKalb, Illinois 60115, USA
⁵¹Northwestern University, Evanston, Illinois 60208, USA
⁵²Indiana University, Bloomington, Indiana 47405, USA
⁵³Purdue University Calumet, Hammond, Indiana 46323, USA
⁵⁴University of Notre Dame, Notre Dame, Indiana 46556, USA
⁵⁵Iowa State University, Ames, Iowa 50011, USA
⁵⁶University of Kansas, Lawrence, Kansas 66045, USA
⁵⁷Kansas State University, Manhattan, Kansas 66506, USA
⁵⁸Louisiana Tech University, Ruston, Louisiana 71272, USA
⁵⁹University of Maryland, College Park, Maryland 20742, USA
⁶⁰Boston University, Boston, Massachusetts 02215, USA
⁶¹Northeastern University, Boston, Massachusetts 02115, USA
⁶²University of Michigan, Ann Arbor, Michigan 48109, USA
⁶³Michigan State University, East Lansing, Michigan 48824, USA
⁶⁴University of Mississippi, University, Mississippi 38677, USA
⁶⁵University of Nebraska, Lincoln, Nebraska 68588, USA
⁶⁶Rutgers University, Piscataway, New Jersey 08855, USA
⁶⁷Princeton University, Princeton, New Jersey 08544, USA
⁶⁸State University of New York, Buffalo, New York 14260, USA
⁶⁹Columbia University, New York, New York 10027, USA
⁷⁰University of Rochester, Rochester, New York 14627, USA
⁷¹State University of New York, Stony Brook, New York 11794, USA
⁷²Brookhaven National Laboratory, Upton, New York 11973, USA
⁷³Langston University, Langston, Oklahoma 73050, USA
⁷⁴University of Oklahoma, Norman, Oklahoma 73019, USA
⁷⁵Oklahoma State University, Stillwater, Oklahoma 74078, USA
⁷⁶Brown University, Providence, Rhode Island 02912, USA
⁷⁷University of Texas, Arlington, Texas 76019, USA
⁷⁸Southern Methodist University, Dallas, Texas 75275, USA
⁷⁹Rice University, Houston, Texas 77005, USA
⁸⁰University of Virginia, Charlottesville, Virginia 22901, USA and
⁸¹University of Washington, Seattle, Washington 98195, USA

(Dated: May 12, 2010)

We present a measurement of direct photon pair production cross sections using 4.2 fb^{-1} of data collected with the D0 detector at the Fermilab Tevatron $p\bar{p}$ Collider. We measure single differential cross sections as a function of the diphoton mass, the transverse momentum of the diphoton system, the azimuthal angle between the photons, and the polar scattering angle of the photons. In addition, we measure double differential cross sections considering the last three kinematic variables in three diphoton mass bins. The results are compared with different perturbative QCD predictions and event generators.

PACS numbers: 13.85.Qk, 12.38.Qk

At a hadron collider, the direct photon pair (DPP) production with large diphoton invariant mass ($M_{\gamma\gamma}$) constitutes a large and irreducible background to searches for the Higgs boson decaying into a pair of photons, for both the Fermilab Tevatron [1] and the CERN LHC experiments [2]. DPP production is also a significant background in searches for new phenomena, such as new heavy resonances [3], extra spatial dimensions [4], or cascade decays of heavy new particles [5]. Thus, precise measurements of the diphoton differential production cross

sections for various kinematic variables and their theoretical understanding are extremely important for future Higgs and new phenomena searches.

In addition, DPP production is interesting in its own right, and is used to check the validity of the predictions of perturbative quantum chromodynamics (pQCD) and soft-gluon resummation methods implemented in theoretical calculations. Measurements involving the diphoton final state have been previously carried out at fixed-target [6, 7] and collider [8–10] experiments. However,

the large integrated luminosity accumulated by the D0 experiment in $p\bar{p}$ collisions at $\sqrt{s} = 1.96$ TeV at the Fermilab Tevatron Collider allows us to perform precise measurements of several observables in kinematic regions previously unexplored, as well as, for the first time, the measurement of double differential cross sections for this process.

The DPP events produced in $p\bar{p} \rightarrow \gamma\gamma + X$ are expected to be dominantly produced via $q\bar{q}$ scattering ($q\bar{q} \rightarrow \gamma\gamma$) and gluon-gluon fusion ($gg \rightarrow \gamma\gamma$) through a quark-loop diagram. In spite of the suppression factor of α_s^2 for $gg \rightarrow \gamma\gamma$ as compared to $q\bar{q} \rightarrow \gamma\gamma$, the former still gives a significant contribution in kinematic regions where the gg parton luminosity is high, especially at low $M_{\gamma\gamma}$. Figure 1 shows the expected contribution to the total DPP rate from $gg \rightarrow \gamma\gamma$, as predicted by the PYTHIA [11] Monte Carlo (MC) event generator with the CTEQ6.1L parton distribution function (PDF) set [12]. In addition, direct photons may result from single or double fragmentation processes of the partons produced in the hard scattering [13, 14]. However, a strict photon isolation requirement significantly reduces the rate for these processes.

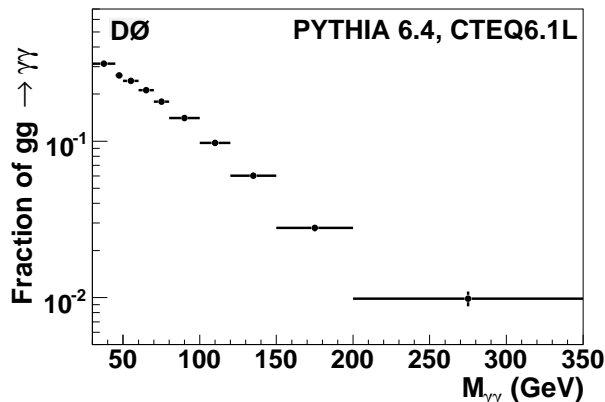


FIG. 1: The fraction of events produced via $gg \rightarrow \gamma\gamma$ scattering relative to total diphoton production as a function of $M_{\gamma\gamma}$, as predicted by the PYTHIA event generator using the CTEQ6.1L PDF set. Photons are required to have transverse momentum $p_T > 21(20)$ GeV for the highest (next-to-highest) p_T photon and pseudorapidity $|\eta| < 0.9$ [15].

In this Letter, we present measurements of the DPP production cross sections using data collected by the D0 experiment from August 2006 to June 2009. The cross sections are measured differentially as a function of $M_{\gamma\gamma}$, the diphoton transverse momentum ($p_T^{\gamma\gamma}$), the azimuthal angle between the photons ($\Delta\phi_{\gamma\gamma}$), and the cosine of the polar scattering angle of the photon in the frame with no net transverse momentum of the diphoton system (defined as $\cos\theta^* = \tanh[(\eta_1 - \eta_2)/2]$, where $\eta_{1(2)}$ is the pseudorapidity of the highest (next-to-highest) p_T photon). These kinematic variables probe different aspects of the DPP production mechanism. For instance, the shapes of the $p_T^{\gamma\gamma}$ and $\Delta\phi_{\gamma\gamma}$ distributions are mostly

affected by initial state gluon radiation and fragmentation effects. In addition, the $M_{\gamma\gamma}$ spectrum is particularly sensitive to potential contributions from new phenomena. The $\cos\theta^*$ distribution probes PDF effects and the angular momentum of the final state, which should be different for QCD-mediated production as compared, for example, to the decay of a spin-0 Higgs boson [13]. The measured cross sections are compared to theoretical predictions from RESBOS [13], DIPHOX [14], and PYTHIA [11]. Both RESBOS and DIPHOX provide next-to-leading order (NLO) predictions in pQCD, however the $gg \rightarrow \gamma\gamma$ contribution is considered only at leading order (LO) in DIPHOX. PYTHIA is a parton shower MC event generator that includes the above processes at LO. In DIPHOX, the explicit parton-to-photon fragmentation functions are included at NLO, while in RESBOS a function approximating rate from the NLO fragmentation diagrams is introduced. Also, only in RESBOS, the effects of soft and collinear initial state gluon emissions are resummed to all orders. This is particularly important for the description of the $p_T^{\gamma\gamma}$ ($\Delta\phi_{\gamma\gamma}$) distribution, which is a δ -function at LO and diverges at NLO as $p_T^{\gamma\gamma} \rightarrow 0$ ($\Delta\phi_{\gamma\gamma} \rightarrow \pi$).

The D0 detector is a general purpose detector discussed in detail elsewhere [16]. The subdetectors most relevant to this analysis are the central tracking system, composed of a silicon microstrip tracker (SMT) and a central fiber tracker (CFT) embedded in a 2 T solenoidal magnetic field, the central preshower detector (CPS), and the calorimeter. The CPS is located immediately before the inner layer of the calorimeter and is formed of approximately one radiation length of lead absorber followed by three layers of scintillating strips. The calorimeter consists of a central section with coverage in pseudorapidity of $|\eta_{\text{det}}| < 1.1$ [15], and two end calorimeters covering up to $|\eta_{\text{det}}| \approx 4.2$. The electromagnetic (EM) section of the calorimeter is segmented longitudinally into four layers (EM*i*, $i = 1, 4$), with transverse segmentation into cells of size $\Delta\eta_{\text{det}} \times \Delta\phi_{\text{det}} = 0.1 \times 0.1$ [15], except EM3 (near the EM shower maximum), where it is 0.05×0.05 . The calorimeter is well-suited for a precise measurement of the energy and direction of electrons and photons, providing an energy resolution of about 3.6% at an energy of 50 GeV and an angular resolution of about 0.01 radians. The energy response of the calorimeter to photons is calibrated using electrons from Z boson decays. Since electrons and photons shower differently in matter, additional corrections as a function of η are derived using a detailed GEANT-based [17] simulation of the D0 detector response. These corrections are largest [(2.0 – 2.5)%] at low photon energies (≈ 20 GeV). The data used in this analysis were collected using a combination of triggers requiring at least two clusters of energy in the EM calorimeter with loose shower shape requirements and varying p_T thresholds between 15 GeV and 25 GeV, and correspond to an integrated luminosity of $4.2 \pm 0.3 \text{ fb}^{-1}$ [18].

Events are selected by requiring two photon candi-

dates with transverse momentum $p_T > 21$ (20) GeV for the highest (next-to-highest) p_T photon candidate and pseudorapidity $|\eta| < 0.9$, for which the trigger requirements are $> 96\%$ efficient. The minimum p_T requirements for the two photon candidates are chosen to be different following theoretical discussions [13, 14] and a previous measurement [10]. The photon p_T is computed with respect to the reconstructed event primary vertex (PV) with the highest number of associated tracks. The PV is required to be within 60 cm of the center of the detector along the beam axis. The PV has a reconstruction efficiency of about 98% and has about 65% probability of being the correct vertex corresponding to the hard $p\bar{p} \rightarrow \gamma\gamma + X$ production.

Photon candidates are formed from clusters of calorimeter cells within a cone of radius $\mathcal{R} = \sqrt{(\Delta\eta)^2 + (\Delta\phi)^2} = 0.4$ around a seed tower [16]. The final cluster energy is then recalculated from the inner core with $\mathcal{R} = 0.2$. The photon candidates are selected by requiring: (i) $\geq 97\%$ of the cluster energy be deposited in the EM calorimeter layers; (ii) the calorimeter isolation $\mathcal{I} = [E_{\text{tot}}(0.4) - E_{\text{EM}}(0.2)]/E_{\text{EM}}(0.2) < 0.10$, where $E_{\text{tot}}(\mathcal{R})$ [$E_{\text{EM}}(\mathcal{R})$] is the total [EM only] energy in a cone of radius \mathcal{R} ; (iii) the p_T scalar sum of all tracks originating from the PV in an annulus of $0.05 < \mathcal{R} < 0.4$ around the EM cluster be < 1.5 GeV; and (iv) the energy-weighted EM shower width be consistent with that expected for an electromagnetic shower. To suppress electrons misidentified as photons, the EM clusters are required to not be spatially matched to significant tracker activity, either a reconstructed track or a density of hits in the SMT and CFT consistent with that of an electron [19]. In the following, this requirement will be referred to as the “track-match veto”.

To further suppress jets misidentified as photons, an artificial neural network (NN) discriminant which exploits differences in tracker activity and energy deposits in the calorimeter and in the CPS between photons and jets is defined [1]. The NN is trained using γ and jet PYTHIA MC samples. The shapes of the NN output (O_{NN}), normalized to unit area and obtained after applying all data selection criteria, are shown in Figure 2, exhibiting a significant discrimination between photons and jets. Photon candidates satisfy the requirement $O_{\text{NN}} > 0.3$, which is $\approx 98\%$ efficient for photons and rejects $\approx 40\%$ of the jets misidentified as photons. The O_{NN} shape is validated in data. For photons a data sample consisting of photons radiated from charged leptons in Z boson decays ($Z \rightarrow \ell^+\ell^-\gamma$, $\ell = e, \mu$) [20] is used. The MC modeling of the O_{NN} shape for jets is validated in a sample of photon candidates selected by inverting the photon isolation ($\mathcal{I} > 0.07$), a requirement that significantly enriches the sample in jets. The data and MC O_{NN} shapes are compared in Figures 2 and 3 and found to be in good agreement.

Finally, the two photon candidates are required to be

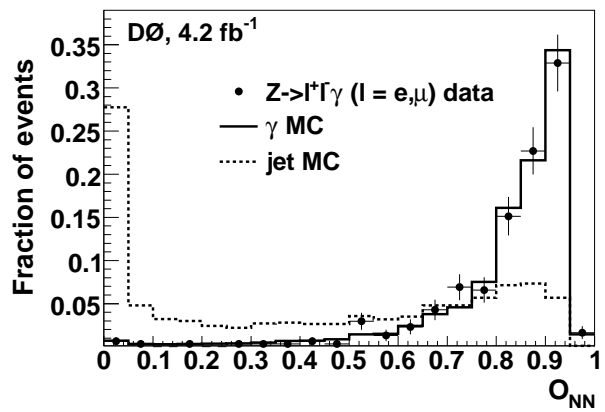


FIG. 2: Comparison of the normalized O_{NN} spectra for photons from DPP MC and $Z \rightarrow \ell^+\ell^-\gamma$ data and for misidentified jets from dijet MC.

spatially separated from each other by a distance in $\eta - \phi$ space $\Delta\mathcal{R} > 0.4$ and to satisfy $M_{\gamma\gamma} > p_T^{\gamma\gamma}$. The latter requirement is satisfied by the majority ($\approx 92\%$) of DPP events and, together with the photon isolation requirements, allows significant suppression of the contribution from the fragmentation diagrams, thus restricting the data-to-theory comparison to the region where the theoretical calculations should have smaller uncertainties [13].

After imposing all requirements, 10938 events with diphoton candidates are selected in data. This sample includes instrumental background contributions from γ +jet and dijet production, where a jet is misidentified as a single photon as a result of fluctuations in the parton fragmentation into a well-isolated neutral meson (π^0 or η) decaying into a final state with two or more photons. An additional smaller background contribution results from Z-boson/Drell-Yan production events $Z/\gamma^* \rightarrow e^+e^-$ (ZDY) in which both electrons are misidentified as photons.

The contribution from ZDY events is estimated using the MC simulation with PYTHIA, normalized to the NNLO cross section [21]. The selection efficiencies determined from the MC simulation are corrected to those measured in the data. On average, each electron has a 2% probability of satisfying the photon selection criteria, mainly due to the inefficiency of the track-match veto requirements. The total ZDY contribution is estimated to be 161 ± 20 events. Backgrounds due to γ +jet and dijet events are estimated from data by using a 4×4 matrix background estimation method [1]. After applying all of the selection criteria described above, a tighter O_{NN} requirement ($O_{\text{NN}} > 0.6$) is used to classify the data events into four categories, depending on whether both photon candidates, only the highest p_T one, only the next-to-highest p_T one, or neither of the two photon candidates pass (p) or fail (f) this requirement. The corresponding number of events

(after subtraction of the estimated ZDY contribution) compose a 4-component vector $(N_{pp}, N_{pf}, N_{fp}, N_{ff})$. The difference in relative efficiencies of the $O_{NN} > 0.6$ requirement between photons and jets allows estimation of the sample composition by solving a linear system of equations: $(N_{pp}, N_{pf}, N_{fp}, N_{ff})^T = \mathcal{E} \times (N_{\gamma\gamma}, N_{\gamma j}, N_{j\gamma}, N_{jj})^T$, where $N_{\gamma\gamma}$ (N_{jj}) is the number of DPP (dijet) events and $N_{\gamma j}$ ($N_{j\gamma}$) is the number of γ +jet events with the (next-to-)highest p_T photon candidate being a photon. The 4×4 matrix \mathcal{E} contains the photon ε_γ and jet ε_{jet} efficiencies, estimated using photon and jet MC samples and validated in data. The efficiencies are parameterized as a function of the photon candidate η and vary within (90 – 95)% for ε_γ and within (66 – 70)% for ε_{jet} . The systematic uncertainty on ε_γ is estimated to be 1.5% from a comparison of the efficiency as a function of η between data and MC using samples of electrons from Z boson decays and photons from radiative Z boson decays. In order to estimate the systematic uncertainty on ε_{jet} , two independent control data samples enriched in jets misidentified as photons are selected, either by inverting the photon isolation variable ($\mathcal{I} > 0.07$), or by requiring at least one track in a cone of $\mathcal{R} < 0.05$ around the photon, while keeping the remaining photon selection criteria unchanged. In both cases the agreement with the MC prediction for ε_{jet} is found to be within 10%, which is taken as the systematic uncertainty. The total number of DPP events is found to be $N_{\gamma\gamma} = 7307 \pm 312(\text{stat.})$, corresponding to an average DPP purity of $\approx 67\%$. Following this procedure, the number of DPP events is estimated in each bin of the four kinematic variables considered ($M_{\gamma\gamma}$, $p_T^{\gamma\gamma}$, $\Delta\phi_{\gamma\gamma}$, and $|\cos\theta^*|$). The largest kinematic dependence of the DPP purity is in terms of $M_{\gamma\gamma}$, with a variation between $\approx 60\%$ at $M_{\gamma\gamma} \approx 40$ GeV and close to 100% for $M_{\gamma\gamma} > 200$ GeV. As a function of the other kinematic variables, the DPP purity varies in the (60 – 70)% range. The relative systematic uncertainty on the purity results from the systematic uncertainties on ε_γ and ε_{jet} , and typically varies within (11–15)%. As a cross-check, the DPP purity was also estimated via a fit to the two-dimensional distribution in data of O_{NN,γ_1} versus O_{NN,γ_2} using templates constructed from photons and jets in MC. The result was found to be in good agreement with that from the 4×4 matrix method.

The estimated number of DPP events per bin is corrected for the DPP event selection efficiency and acceptance. The selection efficiency is calculated using DPP events generated with PYTHIA and processed through a GEANT-based simulation of the D0 detector. In order to accurately model the effects of multiple $p\bar{p}$ interactions and detector noise, data events from random $p\bar{p}$ crossings with a similar instantaneous luminosity spectrum as considered in the data analysis are overlaid on the MC events. These MC events are then processed using the same reconstruction code as for the data. Small differ-

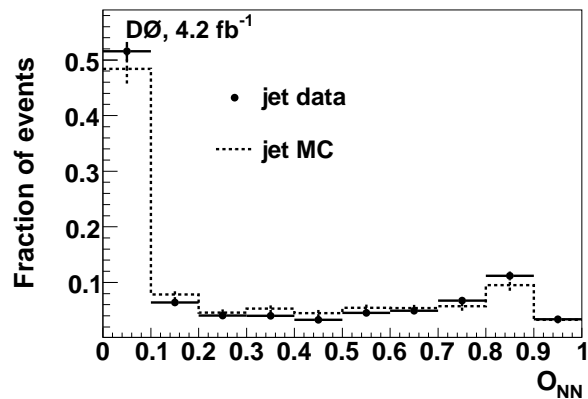


FIG. 3: Comparison of the normalized O_{NN} spectra for jets misidentified as photons in data and in dijet MC.

ences between data and MC in the per-photon selection efficiencies are corrected for with suitable scale factors derived using control samples of electrons from Z boson decays, as well as photons from the radiative Z boson decays. The overall DPP selection efficiency after applying all selection criteria is estimated as a function of the variable of interest. In the case of $p_T^{\gamma\gamma}$, $\Delta\phi_{\gamma\gamma}$, and $|\cos\theta^*|$, it is about 64% with a (2 - 3)% variation across the bins, while for $M_{\gamma\gamma}$, the efficiency grows from about 60% at $30 < M_{\gamma\gamma} < 50$ GeV to 69% at $M_{\gamma\gamma} > 200$ GeV. The total relative systematic uncertainty on the DPP selection efficiency is 4.3%, dominated by the track-match veto and photon O_{NN} selections. The acceptance is calculated using DPP events generated with RESBOS and is driven by the selections in η_{det} ($|\eta_{\text{det}}| < 0.9$, applied to avoid edge effects in the central calorimeter region used for the measurement) and ϕ_{det} (to avoid periodic calorimeter module boundaries [16] that bias the EM cluster energy and position measurements), PV misidentification, photon energy scale, and bin-to-bin migration effects due to the finite energy and angular resolution of the EM calorimeter. The overall DPP acceptance varies within (45–64)% with a relative systematic uncertainty of (4 – 7)%.

The differential cross sections $d\sigma/dM_{\gamma\gamma}$, $d\sigma/dp_T^{\gamma\gamma}$, $d\sigma/d\Delta\phi_{\gamma\gamma}$, and $d\sigma/d|\cos\theta^*|$ are obtained from the number of data events corrected for the background contribution, divided by the trigger, vertex and diphoton selection efficiencies, acceptance, integrated luminosity, and the bin width for each kinematic variable. The measured differential cross sections, compared to the theoretical predictions from RESBOS, are presented in Table I. The average value for each variable in a bin was estimated using RESBOS. The statistical uncertainty δ_{stat} corresponds to the statistical precision on $N_{\gamma\gamma}$ estimated in the 4×4 matrix method, which can be sizable when values of ε_γ and ε_{jet} are numerically close.

Figure 4 shows a comparison of the measured differential cross sections to the theoretical predictions from RESBOS, DIPHOX, and PYTHIA. Systematic uncertainties

in the measured cross sections have large ($> 90\%$) bin-to-bin correlations. There is a common 7.4% normalization uncertainty, resulting from the photon selection criteria (4.3%) and luminosity measurement (6.1%), that is not shown on the data points. The predictions from RESBOS and DIPHOX are computed using the CTEQ6.6M PDF set [12], the DSS set of fragmentation functions [22], and setting renormalization μ_R , factorization μ_F , and fragmentation μ_f scales as $\mu_R = \mu_F = \mu_f = M_{\gamma\gamma}$. The uncertainty due to the scale choice is estimated by simultaneous variation by a factor of two of all scales relative to the default choice and found to be about 10% for $M_{\gamma\gamma}$ and $|\cos\theta^*|$ and up to (15 – 20)% for high $p_T^{\gamma\gamma}$ and low $\Delta\phi_{\gamma\gamma}$. The PDF uncertainty is estimated using DIPHOX and the 44 eigenvectors provided with the CTEQ6.6M PDF set [12] and found to be within (3 – 6)% for all four cross sections. The predictions from PYTHIA are computed with “Tune A” [11], which uses the CTEQ5L PDF set. All theoretical predictions are obtained using diphoton event selection criteria equivalent to those applied in the experimental analysis. In particular, the photon isolation is required to be $E_T^{\text{iso}} = E_T^{\text{tot}}(0.4) - E_T^\gamma < 2.5$ GeV, where $E_T^{\text{tot}}(0.4)$ is the total transverse energy within a cone of radius $\mathcal{R} = 0.4$ centered on the photon, and E_T^γ is the photon transverse energy. For RESBOS and DIPHOX, E_T^{tot} is computed at the parton level, whereas in the case of PYTHIA, it is computed at the particle level. This requirement suppresses the contributions from photons produced in the fragmentation processes and leads to a more consistent comparison with the experimental result. Studies performed using DIPHOX indicate that the contribution to the overall cross section from one- and two-fragmentation processes does not exceed 16% and significantly drops at large $M_{\gamma\gamma}$, $p_T^{\gamma\gamma}$ and small $\Delta\phi_{\gamma\gamma}$ to (1–3)%. In order to allow a direct comparison to the data, the NLO QCD cross sections obtained with RESBOS and DIPHOX are further corrected for contributions from multiple parton interactions and hadronization, both of which affect the efficiency of the isolation requirement. These corrections are estimated using DPP events simulated in PYTHIA using Tunes A and S0 [11]. The corrections vary within (4.0 – 5.5)% as a function of the measured kinematic variables and are consistent for both tunes within 0.5%.

The results obtained show that none of the theoretical predictions considered is able to describe the data well in all kinematic regions of the four variables. RESBOS shows the best agreement with data, although systematic discrepancies are observed at low $M_{\gamma\gamma}$, high $p_T^{\gamma\gamma}$, and low $\Delta\phi_{\gamma\gamma}$. However, the agreement between RESBOS and data is fair at intermediate $M_{\gamma\gamma}$ (50 – 80 GeV), and good at high $M_{\gamma\gamma}$ (> 80 GeV). The large discrepancy between RESBOS and DIPHOX in some regions of the phase space is due to absence of all-order soft-gluon resummation and accounting $gg \rightarrow \gamma\gamma$ contribution just at LO in DIPHOX.

Further insight on the dependence of the $p_T^{\gamma\gamma}$, $\Delta\phi_{\gamma\gamma}$,

TABLE I: The measured differential cross sections in bins of $M_{\gamma\gamma}$, $p_T^{\gamma\gamma}$, $\Delta\phi_{\gamma\gamma}$, and $|\cos\theta^*|$. The columns δ_{stat} and δ_{syst} represent the statistical and systematic uncertainties, respectively. Also shown are the predictions from RESBOS.

$M_{\gamma\gamma}$ (GeV)	$\langle M_{\gamma\gamma} \rangle$ (GeV)	$d\sigma/dM_{\gamma\gamma}$ (pb/GeV)			
		Data	δ_{stat} (%)	δ_{syst} (%)	RESBOS
30 – 45	43.0	3.11×10^{-2}	15	+26/–29	1.94×10^{-2}
45 – 50	47.6	1.74×10^{-1}	11	+19/–19	1.22×10^{-1}
50 – 60	54.7	1.19×10^{-1}	10	+18/–17	1.09×10^{-1}
60 – 70	64.6	7.89×10^{-2}	11	+18/–16	6.82×10^{-2}
70 – 80	74.6	5.61×10^{-2}	10	+17/–15	4.09×10^{-2}
80 – 100	88.6	2.39×10^{-2}	12	+16/–15	2.13×10^{-2}
100 – 120	108.9	1.12×10^{-2}	15	+16/–14	0.98×10^{-2}
120 – 150	132.9	3.65×10^{-3}	23	+16/–14	4.52×10^{-3}
150 – 200	170.7	1.67×10^{-3}	20	+16/–14	1.74×10^{-3}
200 – 350	248.8	3.30×10^{-4}	26	+16/–14	3.53×10^{-4}

$p_T^{\gamma\gamma}$ (GeV)	$\langle p_T^{\gamma\gamma} \rangle$ (GeV)	$d\sigma/dp_T^{\gamma\gamma}$ (pb/GeV)			
		Data	δ_{stat} (%)	δ_{syst} (%)	RESBOS
0.0 – 2.5	1.5	1.92×10^{-1}	15	+18/–19	2.63×10^{-1}
2.5 – 5.0	3.7	3.34×10^{-1}	11	+19/–17	3.30×10^{-1}
5.0 – 7.5	6.2	3.06×10^{-1}	11	+17/–16	2.41×10^{-1}
7.5 – 10.0	8.7	2.38×10^{-1}	12	+18/–17	1.73×10^{-1}
10.0 – 12.5	11.2	1.66×10^{-1}	14	+18/–16	1.28×10^{-1}
12.5 – 15.0	13.7	1.10×10^{-1}	19	+18/–17	9.57×10^{-2}
15.0 – 20.0	17.3	8.80×10^{-2}	15	+18/–17	6.34×10^{-2}
20.0 – 25.0	22.3	6.30×10^{-2}	16	+18/–18	3.98×10^{-2}
25.0 – 30.0	27.3	4.20×10^{-2}	19	+18/–18	2.57×10^{-2}
30.0 – 40.0	34.3	2.99×10^{-2}	13	+18/–17	1.39×10^{-2}
40.0 – 60.0	47.8	7.58×10^{-3}	20	+17/–16	4.72×10^{-3}
60.0 – 100	73.4	9.92×10^{-4}	36	+19/–21	9.20×10^{-4}

$\Delta\phi_{\gamma\gamma}$ (rad)	$\langle \Delta\phi_{\gamma\gamma} \rangle$ (rad)	$d\sigma/d\Delta\phi_{\gamma\gamma}$ (pb/rad)			
		Data	δ_{stat} (%)	δ_{syst} (%)	RESBOS
1.57 – 1.88	1.75	4.32×10^{-1}	20	+19/–21	1.31×10^{-1}
1.88 – 2.20	2.06	5.30×10^{-1}	24	+18/–16	2.70×10^{-1}
2.20 – 2.51	2.38	1.15	16	+18/–16	6.38×10^{-1}
2.51 – 2.67	2.60	2.43	14	+19/–19	1.34
2.67 – 2.83	2.76	3.99	11	+17/–16	2.49
2.83 – 2.98	2.92	6.70	10	+18/–16	5.25
2.98 – 3.14	3.08	1.34×10^1	7	+17/–16	1.33×10^1

$ \cos\theta^* $	$\langle \cos\theta^* \rangle$	$d\sigma/d \cos\theta^* $ (pb)			
		Data	δ_{stat} (%)	δ_{syst} (%)	RESBOS
0.0 – 0.1	0.05	13.8	8	+18/–17	9.22
0.1 – 0.2	0.15	10.0	9	+17/–16	7.96
0.2 – 0.3	0.25	7.78	10	+18/–16	6.99
0.3 – 0.4	0.35	6.38	12	+17/–16	5.90
0.4 – 0.5	0.45	4.77	14	+17/–16	4.54
0.5 – 0.7	0.57	2.35	15	+17/–16	2.16

and $|\cos\theta^*|$ kinematic distributions on the mass scale can be gained through the measurement of double differential cross sections. For this purpose, the differential cross sections as functions of $p_T^{\gamma\gamma}$, $\Delta\phi_{\gamma\gamma}$, and $|\cos\theta^*|$ are measured in three $M_{\gamma\gamma}$ bins: 30 – 50 GeV, 50 – 80 GeV and 80 – 350 GeV. The results are presented in Tables II – IV, corresponding to each of the three $M_{\gamma\gamma}$ inter-

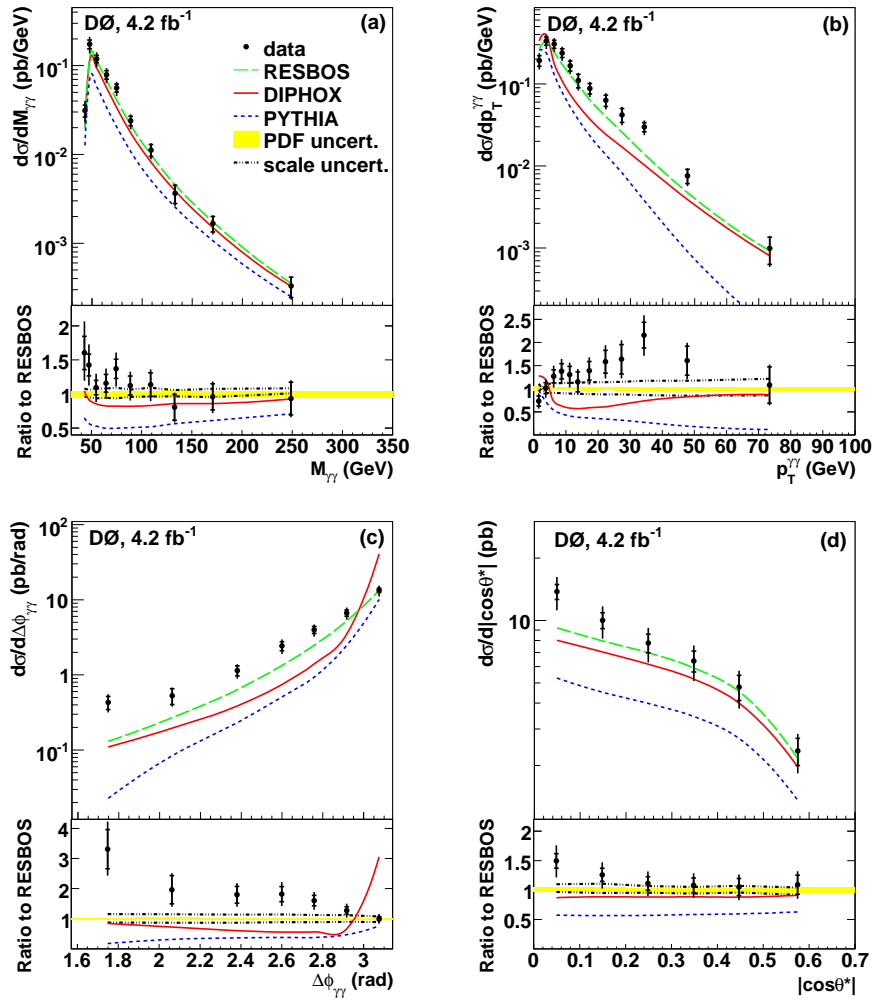


FIG. 4: The measured differential diphoton production cross sections as functions of (a) $M_{\gamma\gamma}$, (b) $p_T^{\gamma\gamma}$, (c) $\Delta\phi_{\gamma\gamma}$, and (d) $|\cos\theta^*|$. The data are compared to the theoretical predictions from RESBOS, DIPHOX, and PYTHIA. The predictions from RESBOS, and DIPHOX use the CTEQ6.6M PDF set [12] and renormalization, factorization, and fragmentation scales $\mu_R = \mu_F = \mu_s = M_{\gamma\gamma}$, while PYTHIA uses the Tune A settings. Theoretical predictions are obtained using the following selections: two photons with $p_T > 21(20)$ GeV, $|\eta| < 0.9$, $30 < M_{\gamma\gamma} < 350$ GeV, $M_{\gamma\gamma} > p_T^{\gamma\gamma}$, $\Delta\mathcal{R} > 0.4$, $\Delta\phi_{\gamma\gamma} > 0.5\pi$, and $E_T^{\text{iso}} < 2.5$ GeV. The ratio of differential cross sections between data and RESBOS are displayed as black points with uncertainties in the bottom plots. The inner line for the uncertainties in data points shows the statistical uncertainty, while the outer line shows the total (statistical and systematic added in quadrature) uncertainty after removing the 7.4% normalization uncertainty. The solid (dashed) line shows the ratio of the predictions from DIPHOX (PYTHIA) to those from RESBOS. In the bottom plots, the scale uncertainties are shown by dash-dotted lines and the PDF uncertainties by shaded regions.

vals. Each table is split into three sub-tables, showing results separately for $d^2\sigma/dM_{\gamma\gamma}dp_T^{\gamma\gamma}$, $d^2\sigma/dM_{\gamma\gamma}d\Delta\phi_{\gamma\gamma}$, and $d^2\sigma/dM_{\gamma\gamma}d|\cos\theta^*|$. The measured cross sections for the $p_T^{\gamma\gamma}$, $\Delta\phi_{\gamma\gamma}$, and $|\cos\theta^*|$ variables in the three mass bins are shown in Figures 5 – 7 and compared to the theoretical predictions. These results confirm that the largest discrepancies between data and RESBOS for each of the kinematic variables originate from the lowest $M_{\gamma\gamma}$ region ($M_{\gamma\gamma} < 50$ GeV). As shown in Figure 1, this is the region where the contribution from $gg \rightarrow \gamma\gamma$ is expected to be largest. The discrepancies between data and RESBOS are reduced in the intermediate $M_{\gamma\gamma}$ region (50 – 80 GeV), and a quite satisfactory description of

all kinematic variables is achieved for the $M_{\gamma\gamma} > 80$ GeV region, the relevant region for the Higgs boson and new phenomena searches. However, it should be pointed out that at the Tevatron, DPP production at high masses is strongly dominated by $q\bar{q}$ annihilation, in contrast with the LHC, where the contribution from gg and qg initiated process will be significant. It remains to be seen whether the addition of NNLO corrections to RESBOS, as done in [23], will improve the description of the high $p_T^{\gamma\gamma}$ (low $\Delta\phi_{\gamma\gamma}$) spectrum at low $M_{\gamma\gamma}$.

In summary, we have presented measurements of single and double differential cross sections for DPP production in $p\bar{p}$ collisions at $\sqrt{s} = 1.96$ TeV. This analysis

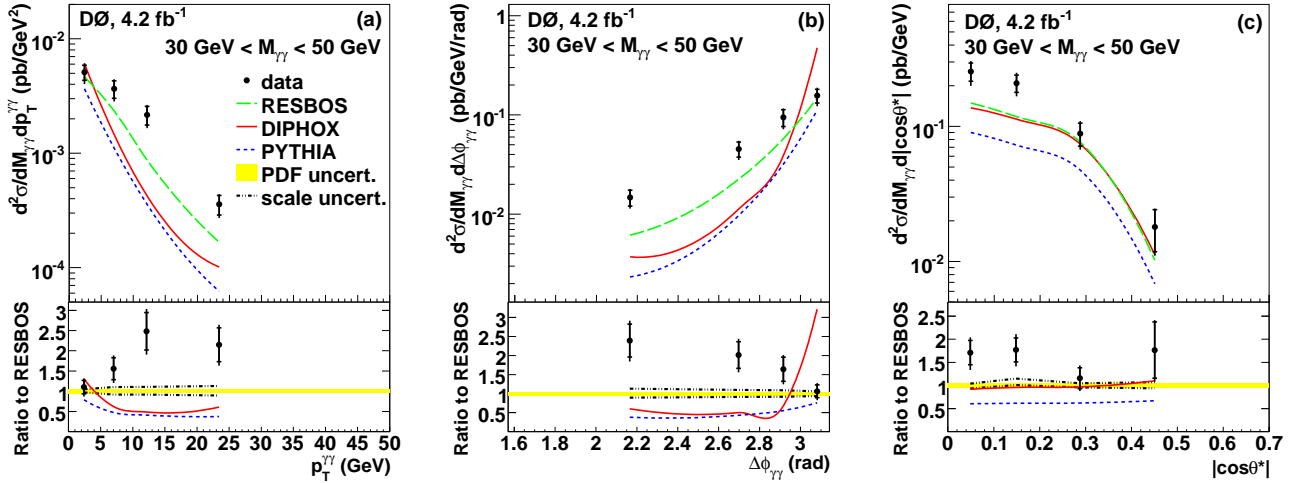


FIG. 5: The measured double differential diphoton production cross sections as functions of (a) $p_T^{\gamma\gamma}$, (b) $\Delta\phi_{\gamma\gamma}$, and (c) $|\cos\theta^*|$ for $30 < M_{\gamma\gamma} < 50$ GeV. The notations for points, lines and shaded regions are the same as in Figure 4.

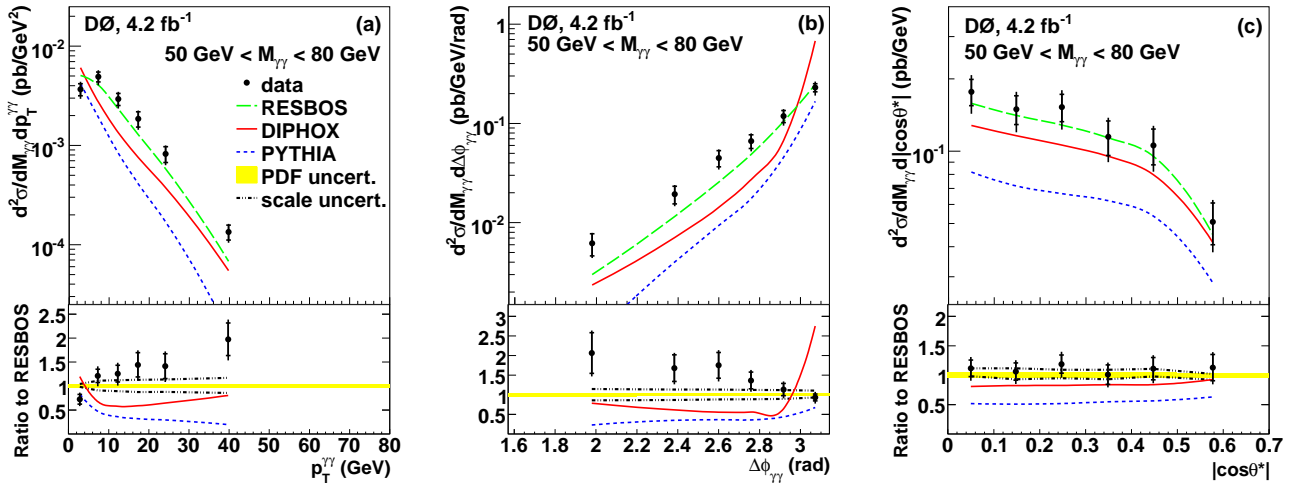


FIG. 6: The measured double differential diphoton production cross sections as functions of (a) $p_T^{\gamma\gamma}$, (b) $\Delta\phi_{\gamma\gamma}$, and (c) $|\cos\theta^*|$ for $50 < M_{\gamma\gamma} < 80$ GeV. The notations for points, lines and shaded regions are the same as in Figure 4.

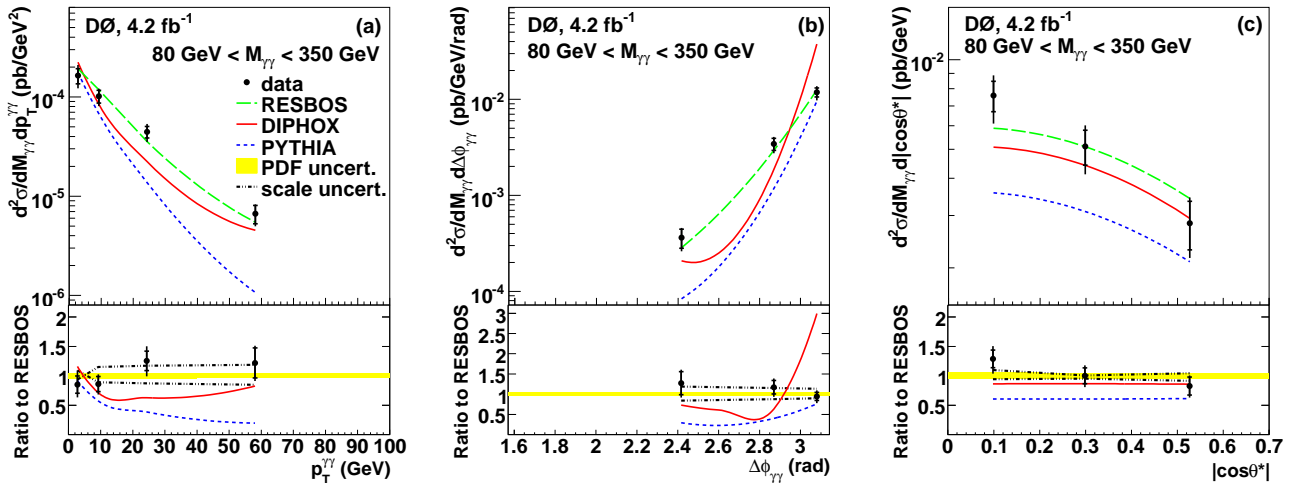


FIG. 7: The measured double differential diphoton production cross sections as functions of (a) $p_T^{\gamma\gamma}$, (b) $\Delta\phi_{\gamma\gamma}$, and (c) $|\cos\theta^*|$ for $80 < M_{\gamma\gamma} < 350$ GeV. The notations for points, lines and shaded regions are the same as in Figure 4.

uses 4.2 fb^{-1} of D0 data, representing a twenty-fold increase in statistics relative to the last published Tevatron results [10]. The measured cross sections are compared to predictions from RESBOS, DIPHOX and PYTHIA, showing the necessity of including higher order corrections beyond NLO as well as the resummation to all orders of soft and collinear initial state gluons. These results allow the tuning of the theoretical predictions for this process, which is of great relevance for improving the sensitivity of searches for the Higgs boson and other new phenomena at the Tevatron and the LHC.

TABLE II: The measured double differential cross sections in bins of $p_T^{\gamma\gamma}$, $\Delta\phi_{\gamma\gamma}$, and $|\cos\theta^*|$, in the region $30 < M_{\gamma\gamma} < 50 \text{ GeV}$. The columns δ_{stat} and δ_{syst} represent the statistical and systematic uncertainties, respectively. Also shown are the predictions from RESBOS.

$p_T^{\gamma\gamma}$ (GeV)	$\langle p_T^{\gamma\gamma} \rangle$ (GeV)	$d^2\sigma/dM_{\gamma\gamma}dp_T^{\gamma\gamma}$ (pb/GeV ²)			
		Data	δ_{stat} (%)	δ_{syst} (%)	RESBOS
0.0 – 5.0	2.4	5.11×10^{-3}	15	+17/-14	4.64×10^{-3}
5.0 – 10.0	7.0	3.65×10^{-3}	18	+16/-14	2.35×10^{-3}
10.0 – 15.0	12.2	2.17×10^{-3}	19	+16/-14	8.72×10^{-4}
15.0 – 50.0	23.4	3.58×10^{-4}	19	+16/-14	1.67×10^{-4}

$\Delta\phi_{\gamma\gamma}$ (rad)	$\langle \Delta\phi_{\gamma\gamma} \rangle$ (rad)	$d^2\sigma/dM_{\gamma\gamma}d\Delta\phi_{\gamma\gamma}$ (pb/GeV/rad)			
		Data	δ_{stat} (%)	δ_{syst} (%)	RESBOS
1.57 – 2.51	2.16	1.48×10^{-2}	18	+16/-14	6.16×10^{-3}
2.51 – 2.83	2.70	4.54×10^{-2}	17	+16/-14	2.25×10^{-2}
2.83 – 2.98	2.92	9.45×10^{-2}	19	+16/-14	5.76×10^{-2}
2.98 – 3.14	3.08	1.57×10^{-1}	16	+16/-14	1.48×10^{-1}

$ \cos\theta^* $ (rad)	$\langle \cos\theta^* \rangle$ (rad)	$d^2\sigma/dM_{\gamma\gamma}d \cos\theta^* $ (pb/GeV)			
		Data	δ_{stat} (%)	δ_{syst} (%)	RESBOS
0.0 – 0.1	0.05	2.55×10^{-1}	15	+17/-14	1.49×10^{-1}
0.1 – 0.2	0.15	2.09×10^{-1}	15	+16/-15	1.18×10^{-1}
0.2 – 0.4	0.28	8.84×10^{-2}	19	+16/-16	7.64×10^{-2}
0.4 – 0.7	0.44	1.80×10^{-2}	35	+19/-15	1.02×10^{-2}

We thank C. Balazs, C.-P. Yuan and J.P. Guillet for their assistance with the theoretical predictions. We also thank F. Siegert and S. Schumann for useful discussions. We thank the staffs at Fermilab and collaborating institutions, and acknowledge support from the DOE and NSF (USA); CEA and CNRS/IN2P3 (France); FASI, Rosatom and RFBR (Russia); CNPq, FAPERJ, FAPESP and FUNDUNESP (Brazil); DAE and DST (India); Colciencias (Colombia); CONACyT (Mexico); KRF and KOSEF (Korea); CONICET and UBACyT (Argentina); FOM (The Netherlands); STFC and the Royal Society (United Kingdom); MSMT and GACR (Czech Republic); CRC Program and NSERC (Canada); BMBF and DFG (Germany); SFI (Ireland); The Swedish Research Council (Sweden); and CAS and CNSF (China).

TABLE III: The measured double differential cross sections in bins of $p_T^{\gamma\gamma}$, $\Delta\phi_{\gamma\gamma}$, and $|\cos\theta^*|$, in the region $50 < M_{\gamma\gamma} < 80 \text{ GeV}$. The notations are the same as in Table II.

$p_T^{\gamma\gamma}$ (GeV)	$\langle p_T^{\gamma\gamma} \rangle$ (GeV)	$d^2\sigma/dM_{\gamma\gamma}dp_T^{\gamma\gamma}$ (pb/GeV ²)			
		Data	δ_{stat} (%)	δ_{syst} (%)	RESBOS
0.0 – 5.0	2.8	3.68×10^{-3}	14	+16/-15	5.07×10^{-3}
5.0 – 10.0	7.3	4.92×10^{-3}	12	+16/-14	4.06×10^{-3}
10.0 – 15.0	12.3	2.93×10^{-3}	14	+16/-14	2.33×10^{-3}
15.0 – 20.0	17.3	1.86×10^{-3}	18	+16/-14	1.29×10^{-3}
20.0 – 30.0	24.1	8.22×10^{-4}	18	+16/-14	5.81×10^{-4}
30.0 – 80.0	39.8	1.34×10^{-4}	17	+16/-14	6.81×10^{-5}

$\Delta\phi_{\gamma\gamma}$ (rad)	$\langle \Delta\phi_{\gamma\gamma} \rangle$ (rad)	$d^2\sigma/dM_{\gamma\gamma}d\Delta\phi_{\gamma\gamma}$ (pb/GeV/rad)			
		Data	δ_{stat} (%)	δ_{syst} (%)	RESBOS
1.57 – 2.20	1.98	6.19×10^{-3}	25	+16/-14	2.99×10^{-3}
2.20 – 2.51	2.38	1.94×10^{-2}	20	+16/-14	1.16×10^{-2}
2.51 – 2.67	2.60	4.49×10^{-2}	19	+16/-14	2.56×10^{-2}
2.67 – 2.83	2.76	6.64×10^{-2}	16	+16/-14	4.87×10^{-2}
2.83 – 2.98	2.92	1.18×10^{-1}	14	+16/-14	1.04×10^{-1}
2.98 – 3.14	3.07	2.30×10^{-1}	10	+16/-14	2.47×10^{-1}

$ \cos\theta^* $ (rad)	$\langle \cos\theta^* \rangle$ (rad)	$d^2\sigma/dM_{\gamma\gamma}d \cos\theta^* $ (pb/GeV)			
		Data	δ_{stat} (%)	δ_{syst} (%)	RESBOS
0.0 – 0.1	0.05	1.77×10^{-1}	13	+16/-14	1.58×10^{-1}
0.1 – 0.2	0.15	1.50×10^{-1}	14	+16/-14	1.41×10^{-1}
0.2 – 0.3	0.25	1.53×10^{-1}	13	+16/-14	1.29×10^{-1}
0.3 – 0.4	0.35	1.15×10^{-1}	16	+16/-14	1.14×10^{-1}
0.4 – 0.5	0.45	1.06×10^{-1}	17	+16/-14	9.52×10^{-2}
0.5 – 0.7	0.58	5.08×10^{-2}	20	+17/-14	4.50×10^{-2}

TABLE IV: The measured double differential cross sections in bins of $p_T^{\gamma\gamma}$, $\Delta\phi_{\gamma\gamma}$, and $|\cos\theta^*|$, in the region $80 < M_{\gamma\gamma} < 350 \text{ GeV}$. The notations are the same as in Table II.

$p_T^{\gamma\gamma}$ (GeV)	$\langle p_T^{\gamma\gamma} \rangle$ (GeV)	$d^2\sigma/dM_{\gamma\gamma}dp_T^{\gamma\gamma}$ (pb/GeV ²)			
		Data	δ_{stat} (%)	δ_{syst} (%)	RESBOS
0.0 – 5.0	2.8	1.64×10^{-4}	17	+20/-24	1.93×10^{-4}
5.0 – 15.0	9.3	1.02×10^{-4}	15	+16/-14	1.18×10^{-4}
15.0 – 40.0	24.3	4.46×10^{-5}	13	+18/-16	3.56×10^{-5}
40.0 – 100	58.1	6.67×10^{-6}	21	+16/-14	5.48×10^{-6}

$\Delta\phi_{\gamma\gamma}$ (rad)	$\langle \Delta\phi_{\gamma\gamma} \rangle$ (rad)	$d^2\sigma/dM_{\gamma\gamma}d\Delta\phi_{\gamma\gamma}$ (pb/GeV/rad)			
		Data	δ_{stat} (%)	δ_{syst} (%)	RESBOS
1.57 – 2.67	2.42	3.63×10^{-4}	22	+18/-16	2.85×10^{-4}
2.67 – 2.98	2.87	3.44×10^{-3}	14	+16/-14	2.94×10^{-3}
2.98 – 3.14	3.08	1.19×10^{-2}	11	+16/-14	1.26×10^{-2}

$ \cos\theta^* $ (rad)	$\langle \cos\theta^* \rangle$ (rad)	$d^2\sigma/dM_{\gamma\gamma}d \cos\theta^* $ (pb/GeV)			
		Data	δ_{stat} (%)	δ_{syst} (%)	RESBOS
0.0 – 0.2	0.10	7.58×10^{-3}	12	+17/-14	5.89×10^{-3}
0.2 – 0.4	0.30	5.11×10^{-3}	13	+16/-14	5.11×10^{-3}
0.4 – 0.7	0.53	2.82×10^{-3}	19	+16/-14	3.42×10^{-3}

-
- [a] Visitor from Augustana College, Sioux Falls, SD, USA.
 [b] Visitor from The University of Liverpool, Liverpool, UK.
 [c] Visitor from SLAC, Menlo Park, CA, USA.
 [d] Visitor from ICREA/IFAE, Barcelona, Spain.
 [e] Visitor from Centro de Investigacion en Computacion - IPN, Mexico City, Mexico.
 [f] Visitor from ECFM, Universidad Autonoma de Sinaloa, Culiacán, Mexico.
 [g] Visitor from Universität Bern, Bern, Switzerland.
-
- [1] V.M. Abazov *et al.* (D0 Collaboration), Phys. Rev. Lett. **102**, 231801 (2009).
 [2] G. Aad *et al.* (ATLAS Collaboration), arXiv:0901.0512 [hep-ex] (2009); G.L. Bayatian *et al.* (CMS Collaboration), J. Phys. G **34**, 995 (2007).
 [3] S. Mrenna and J. Wells, Phys. Rev. D **63**, 015006 (2001), and references therein.
 [4] M.C. Kumar, P. Mathews, V. Ravindran, and A. Tripathi, Phys. Lett. B **672**, 45 (2009).
 [5] G.F. Giudice and R. Rattazzi, Phys. Rep. **322**, 419 (1999).
 [6] E. Bonvin *et al.* (WA70 Collaboration), Z. Phys. C **41**, 591 (1989); Phys. Lett. B **236**, 523 (1990).
 [7] M. Begel, Ph.D. Thesis, University of Rochester (1999), FERMILAB-THESIS-1999-05.
 [8] C. Albajar *et al.* (UA1 Collaboration), Phys. Lett. B **209**, 385 (1988).
 [9] J. Alitti *et al.* (UA2 Collaboration), Phys. Lett. B **288**, 386 (1992).
 [10] F. Abe *et al.* (CDF Collaboration), Phys. Rev. Lett. **70**, 2232 (1993); D. Acosta *et al.* (CDF Collaboration), Phys. Rev. Lett. **95**, 022003 (2005).
 [11] T. Sjöstrand, S. Mrenna, P. Z. Skands, JHEP **0605**, 026 (2006). We use PYTHIA version v6.420 with tune A.
 [12] W.K. Tung *et al.*, JHEP **0702**, 052 (2007).
 [13] C. Balazs, E.L. Berger, S. Mrenna, and C.-P. Yuan, Phys. Rev. D **57**, 6934 (1998); C. Balazs, E.L. Berger, P. Nadolsky, and C.-P. Yuan, Phys. Rev. D **76**, 013009 (2007).
 [14] T. Binoth, J.-Ph. Guillet, E. Pilon, and M. Werlen, Eur. Phys. J. C **16**, 311 (2000).
 [15] The polar angle θ and the azimuthal angle ϕ are defined with respect to the positive z axis, which is along the proton beam direction. Pseudorapidity is defined as $\eta = -\ln[\tan(\theta/2)]$. Also, η_{det} and ϕ_{det} are the pseudorapidity and the azimuthal angle measured with respect to the center of the detector.
 [16] V.M. Abazov *et al.* (D0 Collaboration), Nucl. Instrum. Methods in Phys. Res. A **565**, 463 (2006); M. Abolins *et al.*, Nucl. Instrum. Methods in Phys. Res. A **584**, 75 (2007); R. Angstadt *et al.*, arXiv:0911.2522 [physics.ins-det] (2009), submitted to Nucl. Instrum. Methods in Phys. Res. A.
 [17] R. Brun and F. Carminati, CERN Program Library Long Writeup W5013 (1993); we use GEANT version v3.21.
 [18] T. Andeen *et al.*, FERMILAB-TM-2365 (2007).
 [19] V.M. Abazov *et al.* (D0 Collaboration), Phys. Lett. B **659**, 856 (2008).
 [20] V.M. Abazov *et al.* (D0 Collaboration), Phys. Lett. B **653**, 378 (2007).
 [21] R. Hamberg, W.L. van Neerven, and T. Matsuura, Nucl. Phys. **B359**, 343 (1991) [Erratum-ibid. **B644**, 403 (2002)].
 [22] D. de Florian, R. Sassot and M. Stratmann, Phys. Rev. D **75**, 114010 (2007); Phys. Rev. D **76**, 074033 (2007).
 [23] Q.-H. Cao, C.-R. Chen, C. Schmidt, and C.-P. Yuan, arXiv:0909.2305 [hep-ph] (2009).